(Received 6 May 2026, Accepted 9 June 2026, Scheduled 26 June 2026)

Design of an Enhanced Ultra-Wideband Array MIMO Antenna Based on a Metamaterial and Metasurface Hybrid Decoupling Architecture

Xuemei Zheng[1,*], Linfei Yue[2], and Shengbang Ma[2]

[1] *Key Laboratory of Modern Power System Simulation and Control and Renewable Energy Technology Ministry of Education, Northeast Electric Power University, Jilin, China*
[2] *Northeast Electric Power University, Jilin, China*

ABSTRACT: In the study, a hybrid decoupling architecture (HDA) based on metamaterials and metasurfaces is proposed. Subsequently, an enhanced ultra-wideband (EUWB) two-port multiple-input multiple-output (MIMO) array antenna with miniaturization, high isolation, and low coupling is designed based on the proposed HDA. The antenna size is 48 mm × 32 mm × 1.6 mm with an FR4 dielectric substrate, whose relative dielectric constant is 4.4, and loss tangent is 0.005. The simulated and measured results show that the antenna operates from 1.89 to 14.85 GHz with a bandwidth of 12.96 GHz and relative bandwidth of 154.8%. The port isolation S_{21} is less than −26 dB; the envelope correlation coefficient (ECC) is less than 0.06; the diversity gain (DG) is higher than 9.5; and the maximum gain reaches 7.83 dB. Therefore, the enhanced ultra-wideband two-port MIMO array antenna designed based on HDA exhibits excellent performance and has broad application potential in various scenarios for wireless communications.

1. INTRODUCTION

In recent years, the fusion technology of ultra-wideband (UWB) and multiple-input multiple-output (MIMO) has been widely applied in 5G systems [1]. It enables low-latency, maximum-throughput, and high-efficiency signal transmissions and significantly enhances the channel capacity. Therefore, the research and development of 6G communication systems are inseparable from MIMO technology [2]. For antennas applied in 6G communication systems, compact size, operating bandwidth, isolation, and other related performance indicators are core issues that must be addressed. Numerous scholars have proposed various methods for improving the isolation and bandwidth of compact UWB MIMO antennas. Specifically, these methods include electromagnetic bandgap (EBG) [3, 4] based decoupling structures, defected ground decoupling structures, decoupling networks (DNs) [5, 6], neutralization lines (NLs) [7, 8], decoupling resonators, and cascaded filters.

However, the above decoupling methods are generally suitable for scenarios with low isolation requirements and cannot meet the demands of compact antennas for ultra-high isolation and multi-scenario applications. Therefore, aiming at compact UWB MIMO patch antennas, this study proposes an enhanced UWB MIMO antenna with an efficient hybrid decoupling scheme that integrates metamaterials and metasurfaces. The proposed design achieves the co-design of high port isolation, miniaturization, and ultrawide bandwidth simultaneously. Its operating band explicitly covers the following standard frequency ranges:

5G NR: 1.8–6 GHz

6G extended: 6–15 GHz

UWB: 3.1–10.6 GHz

WiFi 6/6E/7: 2.4/5/6 GHz

V2X: 5.855–5.925 GHz

Drone image transmission: 2.4/5.8 GHz

IoT terminals: 2.4/5 GHz

Compared with existing designs, the proposed scheme synergistically improves the antenna's isolation, bandwidth, and radiation performance through the combined effect of metamaterials and metasurfaces, thus fulfilling the requirements of multi-scenario applications.

The main novelty of this work lies in the proposed HDA that integrates metamaterials and metasurfaces to realize collaborative suppression of surface waves and space waves simultaneously. Different from traditional hybrid decoupling methods, the proposed HDA achieves full-band ultra-high isolation from 1.89 GHz to 14.85 GHz without affecting the operating bandwidth and radiation characteristics. The special geometry, arrangement, and dual decoupling mechanism make it suitable for enhanced ultra-wideband MIMO antenna applications.

* Corresponding author: Xuemei Zheng (zhengxuemei@neepu.edu.cn).

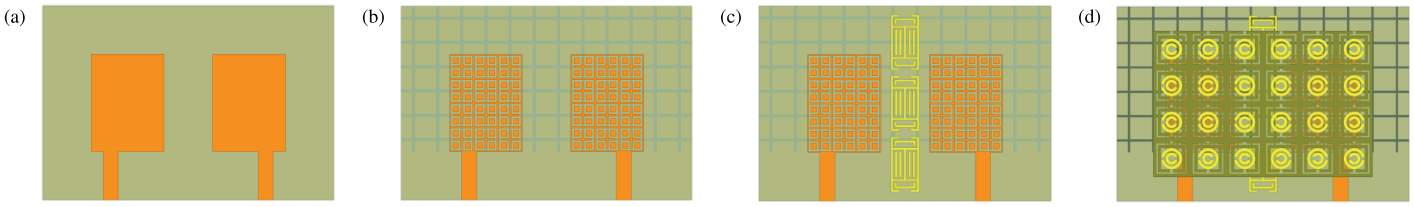

FIGURE 1. EUWB MIMO array antenna design steps: (a) Antenna 1, (b) Antenna 2, (c) Antenna 3, and (d) Antenna 4.

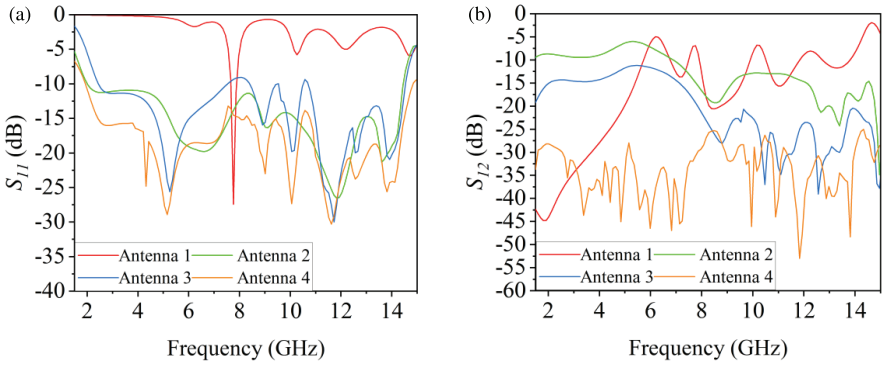

FIGURE 2. Comparison of S-parameters of antennas: (a) S_{11} and (b) S_{12}.

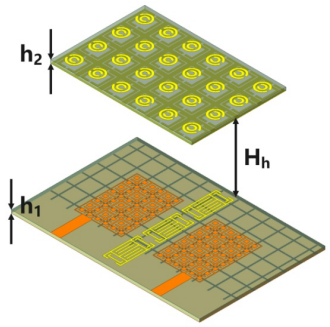

FIGURE 3. 3D structure of the EUWB MIMO array antenna.

2. ANTENNA DESIGN

2.1. Design Process and Analysis of Enhanced Ultra Wideband (EUWB) MIMO Array Antennas

As illustrated in Fig. 1(a), Antenna 1 was first proposed based on a classical rectangular microstrip antenna [9], but its operating bandwidth was only 0.23 GHz, from 7.66 to 7.89 GHz, failing to meet the design objectives for UWB antennas. To address this issue, Antenna 2 was designed by etching a grid-shaped pattern on the radiation patch and periodic strip slots on the ground surface, as shown in Fig. 1(b). As illustrated in Fig. 2(a), the obtained bandwidth is 12.96 GHz, ranging from 1.89 GHz to 14.85 GHz, which is a 56-fold improvement and fully covers the standard UWB from 3.1 GHz to 10.6 GHz [10]. Nevertheless, strong inter-element coupling still exists in the MIMO configuration, with S_{12} ranging from -5 dB to -20 dB, as shown in Fig. 2(b).

As illustrated in Fig. 1(c), Antenna 3 was designed by loading metamaterials between the elements to improve isolation. This preserved the operating bandwidth, enhanced impedance matching, and reduced S_{12} to a maximum of -20 dB from 8 to 15 GHz, verifying the decoupling capability, though severe coupling persisted from 1.8 to 8 GHz. As illustrated in Fig. 1(d), Antenna 4 was proposed based on Antenna 3 with a hybrid decoupling architecture (HDA) for full-band decoupling of surface and space waves. As shown in Fig. 2(a), compared with Antenna 3, the bandwidth of Antenna 4 was not affected by the HDA. As shown in Fig. 2(b), the hybrid architecture maintained the EUWB bandwidth, improved impedance matching, and reduced S_{12} to below -26 dB (minimum -55 dB at 11.8 GHz), endowing the MIMO antenna with high-isolation characteristics.

This experimental result verifies that the proposed HDA can effectively suppress the electromagnetic coupling of the EUWB MIMO antennas without affecting the antenna operating bandwidth and realizes the design target of low coupling and high isolation.

2.2. Structure and Performance Optimization of EUWB MIMO Array Antennas

Based on the analysis results from the previous section, Antenna 4 exhibited optimal bandwidth and decoupling performance. Therefore, this section focuses on analyzing the structural performance. The bandwidth of Antenna 4 exceeds the definition of UWB, so it is referred to as an EUWB MIMO array antenna in this study.

The structure of the proposed EUWB MIMO array antenna consists of two layers: the lower layer is composed of the radiation patches of the EUWB MIMO array antenna and metamaterials for surface-wave decoupling, as shown in Fig. 3. The upper layer comprised an improved dual-opening split-ring resonator (DSRR) [11, 12] metasurface for space wave decoupling. The upper metasurface substrate layer adopts an FR4 dielectric substrate, whose relative dielectric constant is 4.4, and loss tangent is 0.005.

The metamaterials for surface wave decoupling in the lower layer are arranged in a 3×1 configuration, as illustrated in Fig. 4. The upper layer is the metasurface for space-wave decoupling, whose front side is composed of circular dual-opening split-ring resonators, and the back side is composed of square dual-opening split-ring resonators, arranged in a 4×6 configuration, as shown in Fig. 5.

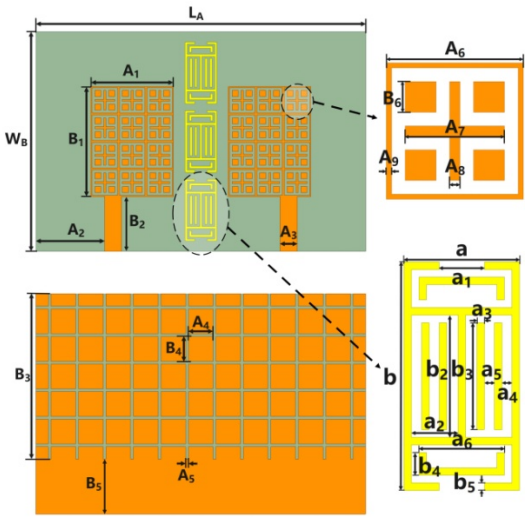

FIGURE 4. Structures of the EUWB MIMO array antenna lower layer.

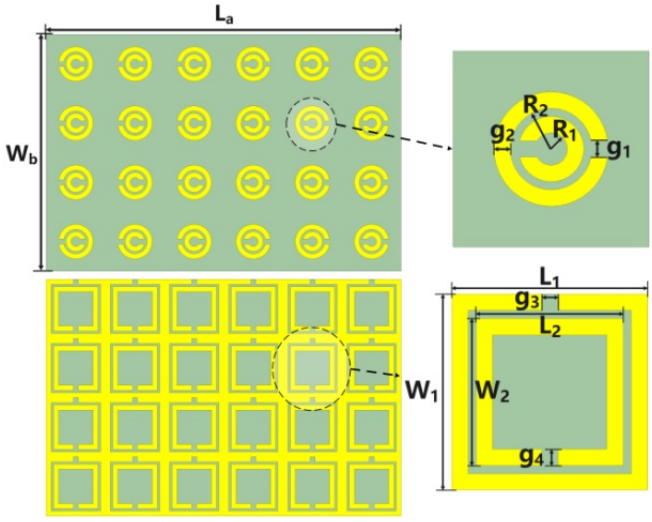

FIGURE 5. Front and back structures of the metasurface on the EUWB MIMO array antenna upper layer.

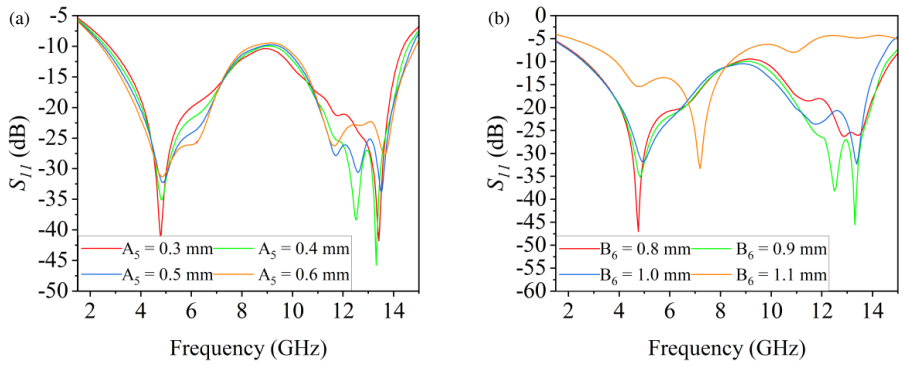

FIGURE 6. Sweep results of A_5 and B_6: (a) A_5 and (b) B_6.

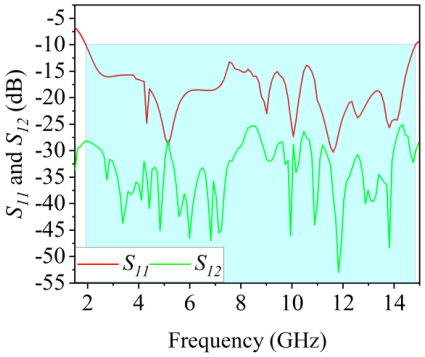

FIGURE 7. S-parameters of the EUWB MIMO array antenna.

As shown in Fig. 6(a), a parameter sweep was subsequently conducted to optimize the antenna performance. First, parameters A_5 and B_6 were swept to explore their effects on S_{11}. For A_5, values of 0.3 mm, 0.4 mm, 0.5 mm, and 0.6 mm were selected. The simulation results show that a larger A_5 leads to poorer impedance matching but a wider bandwidth. A_5 was set to 0.4 mm. For B_6, the sweep uses values of 0.8 mm, 0.9 mm, 1.0 mm, and 1.1 mm. Based on the simulation results, B_6 was determined to be 0.9 mm, as shown in Fig. 6(b).

A parameter sweep was performed for multiple variables in this study. The proposed EUWB MIMO array antenna achieves an operating bandwidth of 12.96 GHz with a relative bandwidth of 154.8%, from 1.89 GHz to 14.85 GHz, fully encompassing the standard UWB of 3.1 GHz to 10.6 GHz. Meanwhile, the antenna achieves an isolation level below −26 dB across the entire band, with a minimum isolation of −55 dB at 11.8 GHz. The S-parameters of the antenna are shown in Fig. 7, and the optimized structural parameters are listed in Table 1.

2.3. Analysis of a Hybrid Metamaterial and Metasurface Decoupling Architecture

Owing to the wide operating frequency range and compact structure of the proposed EUWB MIMO array antenna, a novel decoupling method is proposed for the EUWB MIMO array antenna, which adopts an HDA composed of metamaterials and metasurfaces.

The proposed decoupling architecture is based on dividing the antenna decoupling work into surface-wave decoupling and space-wave decoupling, as shown in Fig. 8.

Two types of metamaterials were used for the HDA. The first type is a rectangular metamaterial dedicated to surface-wave

TABLE 1. Dimensions of the optimized antenna structure.

Parameter	Unit (mm)	Parameter	Unit (mm)	Parameter	Unit (mm)
a_1	12	b_1	16	L_a	36
a_2	10	b_2	8	R_1	0.5
a_3	2.46	b_3	24	R_2	1.25
a_4	3.6	b_4	3.6	L_1	6
a_5	0.4	b_5	8	L_2	4.5
a_6	4	b_6	0.9	g_3	0.5
a_7	2.9	b_7	2	W_b	24
a_8	0.3	h_1	1.6	g_1	0.5
a_9	0.2	h_2	1.6	g_2	0.5
a	4.6	b	9	W_1	6
a_1	1.8	b_1	1.5	W_2	4.5
a_2	1.85	b_2	4.8	g_4	0.5
a_3	0.3	b_3	4.2	h_h	6
a_4	0.4	b_4	0.9	L_A	48
a_5	0.4	b_5	0.3	W_B	32
a_6	3.4				

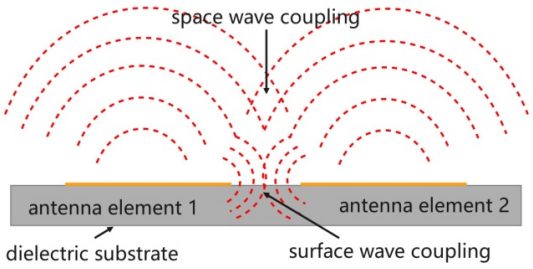

FIGURE 8. Space and surface wave coupling.

decoupling, and the second is a modified double split-ring resonator (DSRR) metamaterial for space-wave decoupling. This section analyzes the metamaterials from two aspects: their S-parameters and equivalent electromagnetic parameters.

To obtain the equivalent electromagnetic parameters of the metamaterials, the Nicolson-Ross-Weir (NRW) [28] method was introduced for parameter extraction. The S-parameter extraction techniques involved in the theoretical calculation are as follows: S_{11} denotes the reflection coefficient [13, 14]. The relationship between S_{12} and the transmission coefficient T can be expressed as follows:

$$S_{12} = Te^{jnk_0d} \tag{1}$$

where K_0 denotes the wave number of the incident wave in free space, and d represents the thickness of the uniform dielectric slab. In addition, the relationship among the S-parameters, refractive index n, and impedance z can be expressed as follows:

$$S_{11} = \frac{R_{01}(1-e^{i2nk_0d})}{1-R_{01}^2e^{i2nk_0d}} \tag{2}$$

$$S_{21} = \frac{(1-R_{01}^2)e^{ink_0d}}{1-R_{01}^2e^{i2nk_0d}} \tag{3}$$

$$R_{01} = (z-1)/(z+1) \tag{4}$$

The expression for impedance z can be derived from the above Eqs. (2) and (3), respectively:

$$Z = \pm\sqrt{\frac{(1+S_{11})^2-S_{21}^2}{(1-S_{11})^2-S_{21}^2}} \tag{5}$$

$$e^{ink_0d} = X \pm i\sqrt{1-X^2} \tag{6}$$

$$X = 1/2[S_{21}(1-S_{11}^2+S_{21}^2)] \tag{7}$$

Because the metamaterial under consideration is a passive dielectric, the parameters z and n in the equations must satisfy the following conditions:

$$\mathrm{Re}(z) \geq 0 \tag{8}$$

$$\mathrm{Im}(n) \geq 0 \tag{9}$$

The formula for calculating the value of the refractive index n is given as follows:

$$n = \frac{1}{k_0d}\{[\mathrm{Im}[In(e^{ink_0d})]+2m\pi]-i\mathrm{Re}[In(e^{ink_0d})]\} \tag{10}$$

where m is an integer related to $\mathrm{Re}(n)$. Finally, two parameters that determine the characteristics of the metamaterial can be derived from these equations. The permeability and permittivity are expressed as follows:

$$\mu = nz \tag{11}$$

$$\varepsilon = n/z \tag{12}$$

As shown in Fig. 9, the electromagnetic characteristics of metamaterial and metasurface units were analyzed under normal surface wave incidence. Ideal periodic boundary conditions (PBCs) were applied in the in-plane direction of the units. A wave port was set in the normal direction to generate vertically incident surface waves. Open boundaries were used to simulate a free-space environment for reliable parameter extraction.

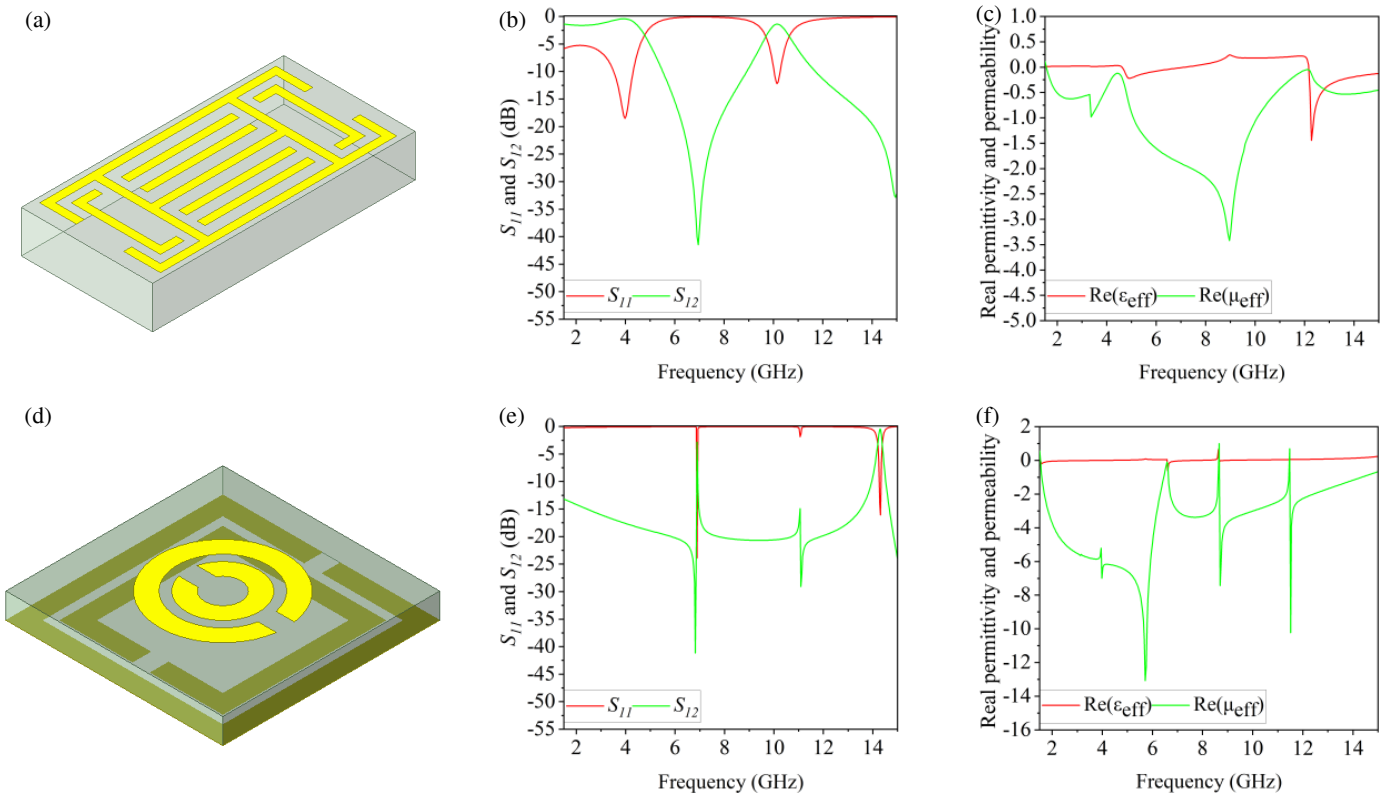

FIGURE 9. Rectangular metamaterial and circular metasurface unit: (a) Model of rectangular metamaterial unit, (b) S-parameters of rectangular metamaterial, (c) equivalent permittivity of rectangular metamaterial, (d) model of circular metasurface unit, (e) S-parameters of circular metasurface, and (f) equivalent permittivity of circular metasurface.

For the metamaterial unit in Fig. 9(a), the reflection coefficient S_{11} in Fig. 9(b) exhibits resonant responses near 4 and 10 GHz. The transmission coefficient S_{12} reaches its minimum value near 7 GHz. According to the effective permeability in Fig. 9(c), the real part of the permeability is negative, from 3.5 to 12.5 GHz. This characteristic helps to form a high-impedance surface. It blocks the propagation of surface waves and restrains the propagation of surface waves along the ground surface.

For the metasurface unit in Fig. 9(d), the reflection coefficient S_{11} in Fig. 9(e) shows resonant responses at 6.5 GHz, 11 GHz, and 14 GHz. The transmission coefficient S_{12} is significantly suppressed from 7 to 11 GHz. Based on the effective permeability in Fig. 9(f), the real part of the permeability remains negative from 2 to 14.5 GHz. It reduces the spatial wave coupling between the antenna elements through phase modulation and scattering effects.

The two units work synergistically from 1.89 to 14.85 GHz. They realized an efficient dual suppression of surface- and spatial-wave coupling. The proposed antenna thus obtains an outstanding full-band decoupling performance. Compared with using only a metamaterial or only a metasurface, the hybrid structure shows a clear synergistic effect. A single metamaterial can suppress surface-wave coupling but has little effect on space waves. A single metasurface can reduce space wave coupling but cannot block surface waves well. Only their combination can suppress both types of coupling at the same time, which brings better isolation than any single decoupling method.

3. EUWB MIMO ARRAY ANTENNA PERFORMANCE ANALYSIS

To evaluate the performance of the MIMO antenna, this study introduces a series of parameters, including Mean Effective Gain (*MEG*) [15], Channel Capacity Loss (*CCL*) [16], Envelope Correlation Coefficient (*ECC*) [17], Diversity Gain (*DG*) [18], gain, and radiation efficiency.

MEG is an indicator for evaluating the signal enhancement capability of an antenna in a specific direction. For a two-element MIMO antenna, it can be calculated using the following formula:

$$MEG_1 = 0.5\eta_{1,rad} = 0.5\left[1 - |S_{11}|^2 - |S_{12}|^2\right] \quad (13)$$

$$MEG_2 = 0.5\eta_{2,rad} = 0.5\left[1 - |S_{21}|^2 - |S_{22}|^2\right] \quad (14)$$

In engineering applications, the requirement for *MEG* is less than -3 dB [19]. The MEG of the antenna designed in this study is less than -6 dB, which satisfies the engineering requirements, as illustrated in Fig. 10(a).

CCL is an indicator of the reduction in channel capacity [31]. For a two-element MIMO antenna, it can be estimated using the following formula:

$$CLL = -\left|\psi^R\right| \quad (15)$$

In engineering practice, the requirement for *CCL* is less than 0.3 bits/s/Hz. The *CCL* of the antenna designed in this study

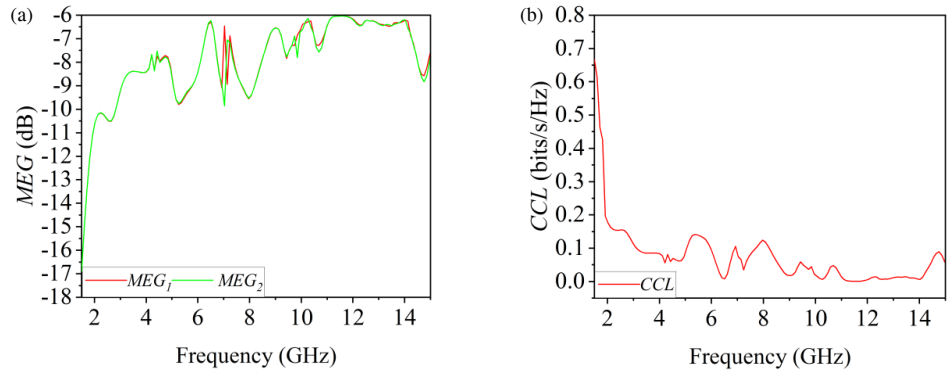

FIGURE 10. *MEG* and *CCL* of the EUWB MIMO array antenna: (a) *MEG* and (b) *CCL*.

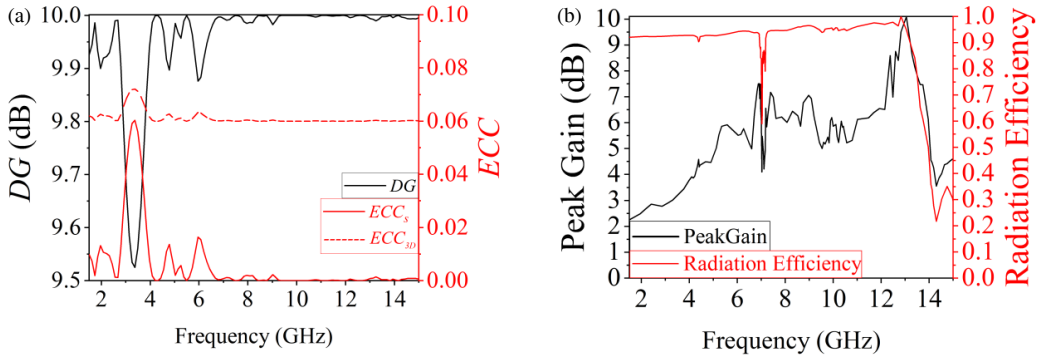

FIGURE 11. *DG*, *ECC*, peak gain and radiation efficiency of the EUWB MIMO array antenna: (a) *DG* and *ECC* and (b) peak gain and radiation efficiency.

was less than 0.2 bits/s/Hz. Therefore, the proposed MIMO antenna system exhibits a relatively small degradation in channel capacity and achieves a favorable performance, as illustrated in Fig. 10(b).

ECC indicates less mutual interference and lower coupling between antenna elements when they operate independently [29]. The formula for calculating ECC_s based on S-parameters is as follows:

$$ECC_s = \frac{\left|S_{11}^* S_{12}' + S_{21}^* S_{22}'\right|^2}{(1-(|S_{11}|^2+|S_{21}|^2))(1-(|S_{22}|^2+|S_{12}|^2))} \quad (16)$$

Due to the low accuracy of S-parameter-based *ECC* calculation for UWB antennas, this study also recalculates the *ECC* using 3D radiation patterns at multiple frequencies and presents a comparison. The formula for calculating ECC_{3D} based on 3D radiation patterns is as follows:

$$ECC_{3D} = \frac{\left|\int\int_{4\pi} \overrightarrow{F_1}(\theta,\phi)\cdot\overrightarrow{F_2}(\theta,\phi)\,d\Omega\right|^2}{[\int\int_{4\pi}\left|\overrightarrow{F_1}(\theta,\phi)\right|^2 d\Omega]\cdot[\int\int_{4\pi}\left|\overrightarrow{F_2}(\theta,\phi)\right|^2 d\Omega]} \quad (17)$$

The ECC_s of the antenna calculated from S-parameters is lower than 0.06, while the ECC_{3D} derived from the 3D radiation pattern is below 0.08. The detailed results are presented in Fig. 11(a). This discrepancy mainly arises because the ECC calculated by S-parameters is obtained under ideal conditions without considering losses, whereas the calculation based on the 3D radiation pattern is relatively accurate.

DG is a parameter that characterizes the diversity performance of MIMO antennas. It can be derived using the following formula [30]:

$$DG = 10 * \sqrt{1-|\mathrm{ECC}|} \quad (18)$$

The *DG* is greater than 9.5, which indicates that the antenna exhibits favorable spatial diversity performance, as illustrated in Fig. 11(a).

The peak gain and radiation efficiency curves of the antenna across the entire operating frequency band are shown in Fig. 11(b). Its gain ranges from 2.5 to 7.83 dB within the band from 4.66 to 15.97 GHz, and the maximum gain of 7.83 dB is obtained at 11.45 GHz. The radiation efficiency is between 70% and 94% over the entire operating frequency band, indicating that most of the energy from the feeder is radiated [20, 21]. This demonstrates that the antenna achieves favorable gain and radiation efficiency across the entire band.

4. EUWB MIMO ARRAY ANTENNA FAR-FIELD RADIATION CHARACTERISTICS ANALYSIS

In this section, the decoupling effect of the HDA is verified by intuitively comparing the surface current distributions of the antenna before and after HDA loading [22].

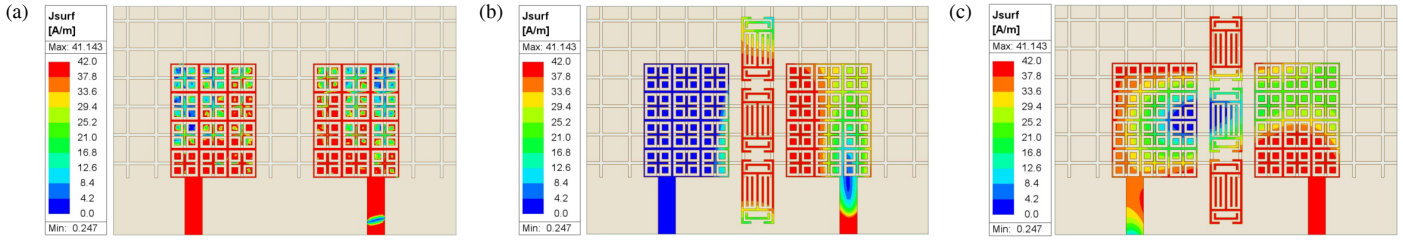

FIGURE 12. Surface current distributions without and with HDA of the EUWB MIMO array antenna @5.6 GHz: (a) Without HDA, (b) without top metasurface, and (c) with HDA.

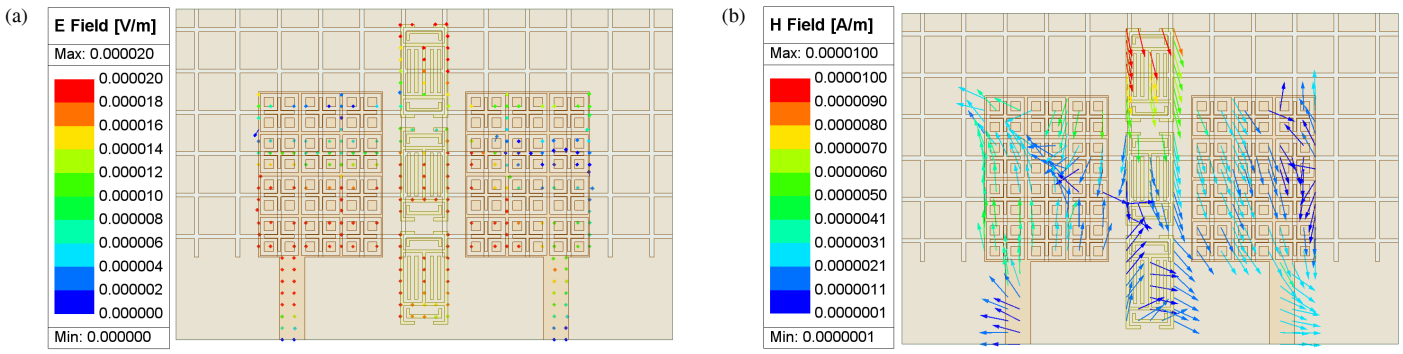

FIGURE 13. E-field and H-field distributions of EUWB MIMO array antenna @5.6 GHz: (a) E-field and (b) H-field.

The influence of the HDA on the antenna radiation characteristics is investigated at 5.6 GHz, which is the frequency point with the strongest inter-element coupling ($S_{12} = -5$ dB) without HDA loading and the typical frequency for verifying the decoupling effect in this study. Therefore, evaluating the stability and omnidirectionality of the radiation characteristics at this frequency is more convincing than at other frequencies [23].

In the absence of the HDA, obvious mutual coupling exists between the MIMO antenna elements. The frequency of 5.6 GHz exhibits the strongest coupling in the entire operating band. At 5.6 GHz, the S_{12} parameter is only -5 dB, leading to poor isolation between elements. Meanwhile, both the surface and space wave coupling reach the most severe state at this frequency. Because 5.6 GHz is the critical frequency with the worst isolation and strongest coupling, it was selected as the typical analysis frequency. Analyzing the field characteristics at this extreme coupling frequency can fully demonstrate the decoupling suppression effect and verify the performance of the proposed HDA.

The color bar on the left side of the figure represents the surface current density (Jsurf) in units of A/m, as shown in Fig. 12(a), Fig. 12(b), and Fig. 12(c), ranging from 0.0 to 42.0 A/m. The red and blue colors correspond to the maximum and minimum current densities, respectively. In the simulation, the maximum observed current density was 41.143 A/m, and the minimum was 0.247 A/m.

As shown in Fig. 12(a), at 5.6 GHz, without the HDA, the current of the excited element is not confined within its radiation structure, as illustrated in Fig. 12(a). Instead, it diffuses significantly into the element gap and ground surface, and induces an obvious induced current on the non-excited adjacent element. It indicates a strong coupling interference between elements, which seriously affects port isolation. As shown in Fig. 12(b), without the space-wave decoupling metasurface structure, the current of the excited element is concentrated in its radiation patch area, but the coupling current between elements is still obvious.

After loading the HDA, the space-wave decoupling metasurface structure, the current of the excited element was concentrated in its radiation patch area, as shown in Fig. 12(c). The coupling current between elements is significantly suppressed, and the induced current on the adjacent element is greatly reduced; thus, the cross-coupling phenomenon is remarkably improved. Meanwhile, the S_{12} parameter at this frequency was optimized from -5 dB to -45 dB, representing an extremely significant improvement in isolation.

The above comparison shows that the designed HDA can effectively block the coupling paths between elements, suppress the current coupling effect, significantly weaken the cross-coupling between antenna elements, and greatly improve the port isolation, thus verifying the effectiveness and superiority of the proposed decoupling scheme over the previous studies [24].

Figure 13 presents the E-field and H-field distributions of the antenna with the proposed HDA at the strongest coupling frequency of 5.6 GHz. As shown in Fig. 13(a), under the effect of the HDA, the E-field energy is effectively confined around the radiation patch of the excited element and the surrounding metasurface, with no continuous coupling path observed between the elements. This indicates that the upper metasurface suppresses space-wave coupling through phase modulation and scattering [25].

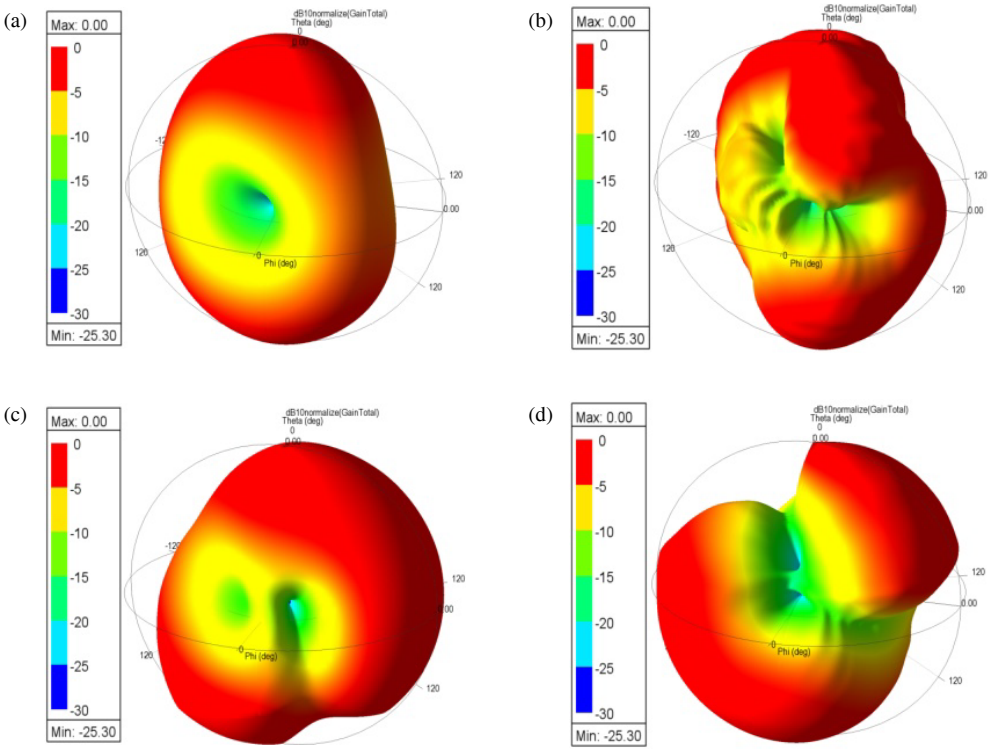

FIGURE 14. 3D radiation patterns of EUWB MIMO array antenna at 5.6 GHz: (a) Without HDA, (b) with HDA, (c) without top metasurface, and (d) with top metasurface.

As shown in Fig. 13(b), the H-field distribution exhibits obvious localization. The high magnetic field region is confined within the element and around the metamaterial structure, and the coupling path along the ground surface is blocked by the high-impedance surface formed by the lower metamaterial. In summary, the HDA achieves efficient decoupling through two synergistic mechanisms: the lower metamaterial suppresses surface-wave coupling, while the upper metasurface suppresses space-wave coupling, resulting in excellent port isolation at 5.6 GHz.

Figure 14 illustrates the evolution of the antenna's 3D radiation patterns at 5.6 GHz through the incorporation of two key structures: HDA and the top metasurface. As shown in Fig. 14(a), the antenna without HDA exhibits a relatively wide main lobe with noticeable back-lobe radiation. After introducing the HDA (Fig. 14(b)), the back lobe is significantly suppressed, and the main lobe becomes more directional, indicating improved front-to-back ratio. Similarly, comparing Figs. 14(c) and 14(d) at 5.6 GHz, the antenna without the top metasurface shows several distinct side lobes [26]. In contrast, with the top metasurface (Fig. 14(d)), the side lobes are effectively reduced, and the overall radiation pattern becomes more concentrated. These observations confirm that HDA plays a critical role in enhancing the antenna's radiation performance at 5.6 GHz.

5. EUWB MIMO ARRAY ANTENNA PROTOTYPE FABRICATION AND PERFORMANCE COMPARISON

In this section, an antenna prototype is fabricated to experimentally verify the proposed HDA and the overall performance of the MIMO antenna. The photographs of the prototype are shown in Fig. 15, where Fig. 15(a) presents the front structure of the prototype, clearly displaying the layout of the radiation patch and feeding port; Fig. 15(b) shows the back structure of the prototype, reflecting the reasonable layout of the ground surface and installation position of the decoupling structure; Fig. 15(c) exhibits the 3D structure of the prototype, intuitively showing the overall spatial layout of the antenna.

In the prototype fabrication, the small corner mechanical standoffs supporting the upper metasurface are made of nylon. It is a low-loss and low-dielectric-constant insulating material widely used in antenna engineering. These nylon standoffs are very small and are only placed at four corners. Therefore, their local dielectric loading effect on impedance matching, operating bandwidth, and port isolation is extremely weak and negligible [27]. The good agreement between simulation and measurement also proves that the standoffs cause no obvious performance degradation or detuning.

The measured data of the prototype were compared with the simulation results, and good agreement was observed between the measured S-parameters, radiation patterns, and simulated results. This not only verifies the accuracy of the simulation model but also confirms the rationality and processability of the antenna design.

The measured results demonstrate that the proposed MIMO antenna achieves an ultra-wide operating bandwidth of 1.89–14.85 GHz, covering the impedance matching condition of S_{11} less than -10 dB and the high isolation requirement of S_{12} less than -25 dB simultaneously within the entire band, as depicted in Fig. 16(b). In particular, at 5.6 GHz, the strongest coupling

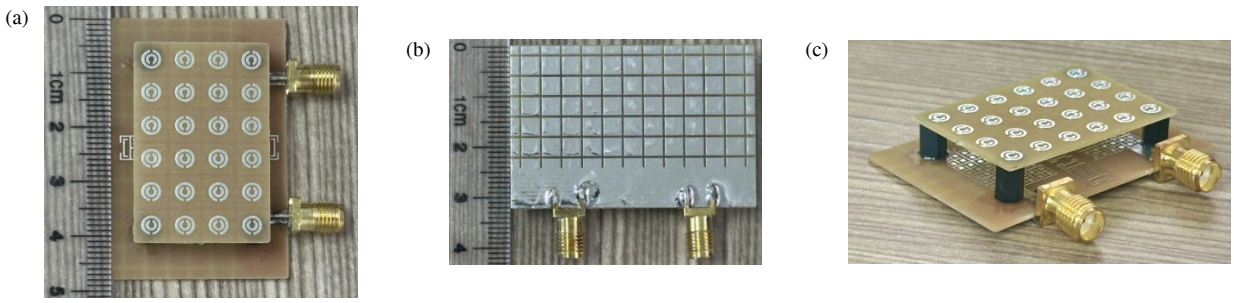

FIGURE 15. Prototype of EUWB MIMO array antenna: (a) Front structure of prototype, (b) back structure of prototype, and (c) 3D structure of prototype.

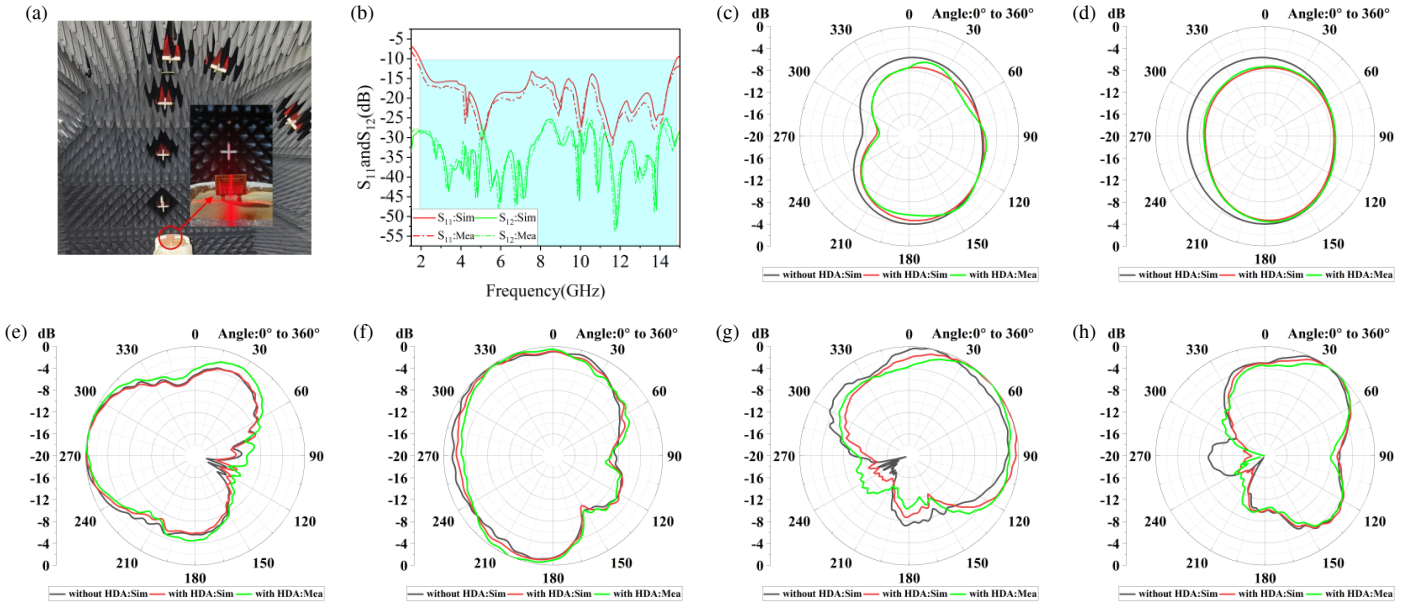

FIGURE 16. Comparison of measured and simulated results for EUWB MIMO array antenna: (a) Experimental setup, (b) comparison of measured and simulated S-parameters, (c) E-plane at 5.6 GHz, (d) H-plane at 5.6 GHz, (e) E-plane at 8.75 GHz, (f) H-plane at 8.75 GHz, (g) E-plane at 11.76 GHz, and (h) H-plane at 11.76 GHz.

frequency point, the port isolation is significantly improved from −5 dB to −45 dB after HDA loading, which fully illustrates that the proposed hybrid decoupling structure provides excellent decoupling performance and fully meets the design target of high isolation for UWB MIMO antennas.

Furthermore, to verify the influence of the decoupling structure on the radiation performance, the radiation patterns of the antenna with and without HDA loading at typical frequency points are compared. As shown in Fig. 16, a comprehensive comparison between the measured and simulated results of the EUWB MIMO array antenna is presented. Fig. 16(a) illustrates the experimental setup employed for antenna performance testing, including the test environment and related measurement equipment. Fig. 16(b) shows the comparison of the measured and simulated S-parameters, which reflect good consistency in impedance matching and port isolation.

To investigate the radiation characteristics of the antenna, three typical frequencies of 5.6 GHz, 8.75 GHz, and 11.76 GHz are selected for analysis. Fig. 16(c) and Fig. 16(d) show the measured and simulated Eplane and Hplane radiation patterns at 5.6 GHz. Fig. 16(e) and Fig. 16(f) show the measured and simulated Eplane and Hplane radiation patterns at 8.75 GHz. Fig. 16(g) and Fig. 16(h) show the measured and simulated Eplane and Hplane radiation patterns at 11.76 GHz. From the comparison, it can be concluded that the measured radiation patterns are highly consistent with the simulated results. No obvious distortion is observed in the main-beam direction, beamwidth, or side-lobe level in both Eplane and Hplane. This indicates that the influence of the decoupling structure on the antenna radiation pattern, gain distribution, and radiation stability is negligible, further verifying the effectiveness and robustness of the proposed HDA.

A brief parameter tolerance analysis was carried out to evaluate the robustness of the proposed antenna against fabrication errors and dielectric constant deviations. Key dimensional parameters were perturbed by ±0.02 mm, while the relative permittivity of the FR4 substrate was varied from 4.38 to 4.42. Simulation results show that the antenna performance remains almost unchanged within typical manufacturing tolerances. The hybrid decoupling architecture maintains high isolation and stable radiation characteristics, demonstrating robustness for practical fabrication and mass production.

TABLE 2. Comparison between the proposed antenna and other antennas.

Reference	Size (mm)	Bandwidth (GHz)	Isolation (dB)	Ports number	ECC	Peak Gain (dBi)	Diversity Gain (dBi)
[5]	140 ∗ 70 ∗ 1.6	6.4–7.1	18	4	0.025	6.4	NG*
[6]	20 ∗ 30 ∗ 1.6	3.01–12.34	22	2	0.0025	5.5	9.99
[7]	36 ∗ 27 ∗ 1.6	12.1–13.99	18.8	2	0.004	6.65	9.98
[10]	75 ∗ 75 ∗ 1.6	3.5–3.8	30	4	0.002	4.8	9.95
[11]	54 ∗ 54 ∗ 1.6	3–11	15	4	0.02	2.83	NG*
[12]	40 ∗ 24 ∗ 1.6	3.1–10.9	15	2	0.2	5	NG*
[13]	50 ∗ 28 ∗ 1.6	2.8–11.5	18	2	0.05	NG*	9.94
[14]	70 ∗ 150 ∗ 1.6	2.5–3.6	15	8	0.02	NG*	NG*
[15]	55 ∗ 26 ∗ 1.6	3.1–12.3	20	2	0.12	4	NG*
[16]	95 ∗ 60 ∗ 1.6	2.4–4.5	18	2	0.15	NG*	NG*
[17]	91 ∗ 38 ∗ 1.6	2.8–10	22	2	0.05	6	NG*
This work	48 ∗ 32 ∗ 1.6	1.89–14.85	26	2	0.06	7.83	9.8
NG* means that this performance is not provided in the paper.							

In conclusion, the measured results were in good agreement with the simulations, and all indicators of the antenna met the design objectives. A good balance among the ultra-wide operating bandwidth, high port isolation, and stable radiation characteristics was achieved. Meanwhile, a comparison with other studies was conducted, as shown in Table 2, fully demonstrating that the designed MIMO antenna possesses high practical engineering application value.

6. CONCLUSIONS

In this study, we propose a novel HDA based on metamaterials and metasurfaces. The proposed HDA differs from existing hybrid decoupling structures in decoupling mechanism, structural geometry, and broadband applicability. It realizes collaborative decoupling of surface waves and space waves and obtains high isolation performance in a UWB range.

An enhanced two-port UWB MIMO array antenna is designed using the proposed HDA, which achieves comprehensive performance in terms of miniaturization, high isolation, and low coupling. Owing to the integrated decoupling design of metamaterials and metasurfaces, the antenna exhibits excellent decoupling capability and stable radiation characteristics. The antenna operates in the frequency range from 1.89 GHz to 14.85 GHz and covers multiple application fields, including UWB, Wi-Fi 6/6E/7, vehicle-mounted V2X, UAV image transmission, and the Internet of Things (IoT) terminals. It boasts advantages such as excellent performance, simple structure, low cost, and easy processing, with significant engineering application value, effectively addressing the inherent defects of traditional decoupling structures.

The proposed antenna has limitations in structural complexity and profile height. In addition, the rigid FR4 substrate limits its flexible applications. In future work, a simplified, low-profile, and flexible design will be studied, and multi-port MIMO antennas will be developed for 6G and multi-scenario applications.

ACKNOWLEDGEMENT

This paper was funded by the National Natural Science Foundation of China (61803356) and also supported by the Jilin Provincial Department of Education Science Research Project, with the project number JJKH20261429KJ.

REFERENCES

[1] Alsaab, N. and M. Shaban, "Design and realization of a multiband, high-gain, and high-isolation MIMO antenna for 5G mmWave communications," *Applied Sciences*, Vol. 15, No. 12, 6857, 2025.

[2] Khan, O., S. Khan, S. N. K. Marwat, N. Gohar, M. Bilal, and M. Dalarsson, "A novel densely packed 4 × 4 MIMO antenna design for UWB wireless applications," *Sensors*, Vol. 23, No. 21, 8888, 2023.

[3] Savcı, H. S., "A four element stringray-shaped MIMO antenna system for UWB applications," *Micromachines*, Vol. 14, No. 10, 1944, 2023.

[4] Chutchavong, V., W. Chanwattanapong, N. Wongsin, P. Rakluea, M. Tangjitjetsada, C. Rakluea, C. Mahatthanajatuphat, and P. Akkaraekthalin, "A flexible and compact UWB MIMO antenna with dual-band-notched double U-shaped slot on mylar® polyester film," *Electronics*, Vol. 14, No. 17, 3363, 2025.

[5] Ghiat, A., J. R. Pérez, R. P. Torres, A. Tribak, and J. Terhzaz, "A multiple-input multiple-output antenna with metamaterial enhancement for 5G channel sounding in the upper 6 GHz band," *Electronics*, Vol. 14, No. 7, 1339, 2025.

[6] Tighilt, Y., C. Bensid, D. Sayad, S. Mekki, R. Zegadi, M. L. Bouknia, I. Elfergani, P. Singh, J. Rodriguez, and C. Zebiri, "Low-profile UWB-MIMO antenna system with enhanced isolation using parasitic elements and metamaterial integration," *Electronics*, Vol. 12, No. 23, 4852, 2023.

[7] Zheng, X., Z. Zhao, Y. Zhang, T. Zhang, A. Gui, and H. Wu, "A low-coupling broadband MIMO array antenna design for Ku-band based on metamaterials," *Journal of Electromagnetic Engineering and Science*, Vol. 24, No. 6, 666–673, 2024.

[8] Zheng, X., Z. Zhao, Y. Pan, and T. Zhang, "Design of a miniaturized symmetrical E-shaped MIMO antenna with low cou-

pling," *Applied Computational Electromagnetics Society Journal (ACES)*, Vol. 39, No. 12, 1051–1058, 2024.

[9] Ramanathan, K., S. Gopalakrishnan, and T. Chandrakanthan, "Miniaturized dual and quad port MIMO antenna variants featuring elevated diversity performance for UWB and 5G-midband applications," *Micromachines*, Vol. 16, No. 6, 716, 2025.

[10] Khan, A. A., Z. Wang, D. Li, A. Aburas, A. Ahmed, and A. Aburas, "Metamaterial-enhanced MIMO antenna for multi-operator ORAN indoor base stations in 5G sub-6 GHz band," *Applied Sciences*, Vol. 15, No. 13, 7406, 2025.

[11] Chen, L.-Y., W.-S. Zhou, J.-S. Hong, and M. Amin, "A compact Eight-port CPW-fed UWB MIMO antenna with Band-notched characteristic," *Applied Computational Electromagnetics Society Journal (ACES)*, Vol. 35, No. 8, 887–892, 2020.

[12] Alsath, M. G. N. and M. Kanagasabai, "Compact UWB monopole antenna for automotive communications," *IEEE Transactions on Antennas and Propagation*, Vol. 63, No. 9, 4204–4208, 2015.

[13] Ibrahim, A. A., J. Machac, and R. M. Shubair, "Compact UWB MIMO antenna with pattern diversity and band rejection characteristics," *Microwave and Optical Technology Letters*, Vol. 59, No. 6, 1460–1464, 2017.

[14] Abdullah, M., S. H. Kiani, and A. Iqbal, "Eight element multiple-input multiple-output (MIMO) antenna for 5G mobile applications," *IEEE Access*, Vol. 7, 134 488–134 495, 2019.

[15] Toktas, A. and A. Akdagli, "Compact multiple-input multiple-output antenna with low correlation for ultra-wide-band applications," *IET Microwaves, Antennas & Propagation*, Vol. 9, No. 8, 822–829, 2015.

[16] Wu, Y.-T. and Q.-X. Chu, "Dual-band multiple input multiple output antenna with slitted ground," *IET Microwaves, Antennas & Propagation*, Vol. 8, No. 13, 1007–1013, 2014.

[17] Jusoh, M., M. F. B. Jamlos, M. R. Kamarudin, and M. F. B. A. Malek, "A MIMO antenna design challenges for UWB application," *Progress In Electromagnetics Research B*, Vol. 36, 357–371, 2012.

[18] Battaglia, G. M., G. G. Bellizzi, A. F. Morabito, G. Sorbello, and T. Isernia, "A general effective approach to the synthesis of shaped beams for arbitrary fixed-geometry arrays," *Journal of Electromagnetic Waves and Applications*, Vol. 33, No. 18, 2404–2422, 2019.

[19] Thotakura, H., R. Gogineni, K. S. Rao, C. K. Kumar, R. B. Sadineni, and S. Mandava, "A miniaturized highly isolated two port triple band-notched UWB MIMO antenna verified by characteristic mode analysis," *Progress In Electromagnetics Research C*, Vol. 160, 133–142, 2025.

[20] Salman, L. A. and K. M. Gatea, "Highly-miniaturized broadband MIMO antennas for WLAN/WiMAX /5G and UWB communications," *Progress In Electromagnetics Research B*, Vol. 115, 120–133, 2025.

[21] El Tayeb, M. M., D. A. E. H. Salem, A. R. Mahmoud, I. M. Ibrahim, A. J. A. Al-Gburi, and M. H. M. Mahmoud, "A compact 4-ports UWB MIMO antenna with WiMAX and WLAN band rejection characteristics," *Progress In Electromagnetics Research C*, Vol. 160, 9–19, 2025.

[22] El Atrash, M., M. S. Khalil, W. A. Mahmoud, and M. A. Addalla, "A low-profile fully fabric high isolation dual-port MIMO antenna for UWB wearable applications," *IEEE Transactions on Antennas and Propagation*, Vol. 74, No. 5, 3971–3979, 2026.

[23] Liu, G.-Y., K. W. Leung, and N. Yang, "Compact radiation-pattern-decoupled MIMO antenna with different radiation directions," *IEEE Transactions on Antennas and Propagation*, Vol. 73, No. 11, 8561–8573, 2025.

[24] Wang, H., Q. Zheng, Q. Li, and X.-X. Yang, "Isolation improvement and bandwidth enhancement of dual-band MIMO antenna based on metamaterial wall," *IEEE Antennas and Wireless Propagation Letters*, Vol. 24, No. 5, 1144–1148, 2025.

[25] Xue, Y., C. Mao, L. Zhang, R. Tafazolli, and A. Kishk, "Broadband circularly polarized helical antenna decoupling for massive MIMO applications," *IEEE Antennas and Wireless Propagation Letters*, Vol. 24, No. 10, 3515–3519, 2025.

[26] Patil, K. D., D. M. Yadav, and J. Kulkarni, "Smart sensor platform for MIMO antennas with gain and isolation enhancement using metamaterial," *Electronics*, Vol. 14, No. 14, 2892, 2025.

[27] Chutchavong, V., W. Chanwattanapong, N. Wongsin, P. Rakluea, M. Tangjitjetsada, C. Rakluea, C. Mahatthanajatuphat, and P. Akkaraekthalin, "A flexible and compact UWB MIMO antenna with dual-band-notched double U-shaped slot on mylar® polyester film," *Electronics*, Vol. 14, No. 17, 3363, 2025.

[28] Nicolson, A. M. and G. F. Ross, "Measurement of the intrinsic properties of materials by time-domain techniques," *IEEE Transactions on Instrumentation and Measurement*, Vol. 19, No. 4, 377–382, 1970.

[29] Blanch, S., J. Romeu, and I. Corbella, "Exact representation of antenna system diversity performance from input parameter description," *Electronics Letters*, Vol. 39, No. 9, 705–707, 2003.

[30] Jamaly, N., P.-S. Kildal, and J. Carlsson, "Compact formulas for diversity gain of two-port antennas," *IEEE Antennas and Wireless Propagation Letters*, Vol. 9, 970–973, 2010.

[31] Shin, H. and J. H. Lee, "On the capacity of MIMO wireless channels," *IEICE Transactions on Communications*, Vol. E87-B, No. 3, 671–677, 2004.

[32] Zheng, X. and A. Gui, "Compact gap-coupled circularly polarized broadband metasurface antenna based on characteristic mode analysis," *Progress In Electromagnetics Research Letters*, Vol. 129, 1–8, 2026.